Three-dimensional effects associated with the low-frequency breathing motion of a turbulent separation bubble

Ben Steinfurth[1,*], Carolina Cura[1], Julien Weiss[1]

1: Chair of Aerodynamics, TU Berlin, Germany
*Corresponding author: ben.steinfurth@tu-berlin.de

Keywords: Stereoscopic PIV, (Spectral) Proper Orthogonal Decomposition, Low-frequency dynamics of turbulent separation bubbles

ABSTRACT

In this article, we address the low-frequency dynamics of a turbulent separation bubble (TSB) with a mean length of $L_\text{b} \approx 0.18$ m that occurs in a one-sided diffuser at an inflow velocity of $U_\infty = 20$ m/s. Distinct low-frequency content at Strouhal numbers of $\mathcal{O}(f L_\text{b}/U_\infty) = 0.01$ is detected through time-resolved wall pressure measurements. By applying Spectral Proper Orthogonal Decomposition to velocity fluctuations in the diffuser symmetry plane, these pressure fluctuations can be linked to a large-scale longitudinal contraction/expansion motion falling into the same frequency range. Further velocity field measurements in cross-sections of one diffuser half-plane indicate that the mean flow field of the TSB is characterized by a near-surface outward-directed velocity component and a large-scale streamwise side wall vortex. During the expanded TSB state, however, these flow features are suppressed as the streamwise velocity is temporarily increased near the side wall but reduced near the symmetry plane. The results presented in this article suggest that the low-frequency *breathing* motion is a highly three-dimensional phenomenon. Future studies should address the associated complex dynamics that are shown to be governed by aperiodic events of temporary TSB expansion in this paper.

1. Introduction

Confined near-wall regions of separated flow, or separation bubbles, are known to exhibit a variety of unsteady mechanisms that are manifested in pressure and velocity fluctuations at different time scales. Three frequency regimes can be distinguished by means of the related Strouhal numbers $St = (f L_\text{b})/U_\infty$ where f is the frequency, L_b a characteristic length of the separation bubble and U_∞ a reference velocity. First, high-frequency broadband fluctuations, driven by turbulent motion, are observed at $St \to 1$. Second, the development, merging and convection of vortex structures inside the separated shear layer are associated with medium-frequency unsteadiness ($St = 0.3, \dots, 0.5$). And third, large-scale deformations of the entire separation bubble are reflected in low-frequency fluctuations ($St < 0.2$).

Typically referred to as flapping or *breathing* motion, unsteady dynamics falling into the latter category have been reported for separation bubbles subject to various boundary conditions (Weiss et al., 2021). This phenomenon is well documented in high-Mach-number flows where low-frequency unsteadiness in the range $St = 0.02, \ldots, 0.05$ is linked to strong pressure and thermal loads in separated shock-wave/boundary layer interactions (SBLIs), e.g. by Dussauge et al. (2006) and Clemens & Narayanaswamy (2014). At subsonic speeds, low-frequency unsteadiness at $St = 0.1, \ldots, 0.2$ has been mostly investigated in flow cases where separation is induced by the surface geometry, for instance on backward-facing steps (Eaton & Johnston, 1982; Driver et al., 1987), blunt plates (Kiya & Sasaki, 1983; Cherry et al., 1984), or vertical fences (Hudy et al., 2003).

Much less is known about the unsteadiness that occurs in low-speed, pressure-induced separated regions where the boundary layer detaches from a smooth surface because of an adverse pressure gradient (APG) instead of a geometric singularity. Laminar separation bubbles (LSBs) are known to flap or burst at low frequency, though the mechanism sustaining this motion and the associated range of frequencies are still subject to debate (Hain et al., 2009; Marxen & Henningson, 2011; Michelis et al., 2017). Even less data have been gathered in the case of pressure-induced turbulent separation bubbles (TSBs) where, contrary to LSBs, the boundary layer is already turbulent at separation. Nevertheless, several authors indicate the possible presence of low-frequency unsteadiness in the range $St = 0.01, \ldots, 0.1$ (Dianat & Castro, 1991; Na & Moin, 1998; Camussi et al., 2008; Weiss et al., 2015; Fang & Tachie, 2020). Recently, Weiss and co-workers investigated the low-frequency behavior of a family of pressure-induced TSBs in a dedicated low-speed wind tunnel featuring a combination of an APG and a favourable pressure gradient (FPG) (Weiss et al., 2015; LeFloc'h et al., 2020). Although the nominal speed was only $U_\infty = 25\,\mathrm{m/s}$, coherent low-frequency dynamics reminiscent of high-speed, SBLI-induced TSBs were observed through pressure fluctuations at $St \approx 0.01$. These fluctuations were also shown to be associated with a significant contraction and expansion (*breathing*) of the entire TSB (Mohammed-Taifour & Weiss, 2016). Contrary to the aforementioned experiments, no significant *breathing* of the TSB could be observed in direct numerical simulations (DNS) performed by Wu et al. (2020). On the other hand, when reattachment was solely caused by turbulent diffusion (APG-only configuration), low-frequency unsteadiness at a relatively high Strouhal number compared to other studies occurred ($St \approx 0.4$).

In summary, the low-frequency *breathing* motion of pressure-induced TSBs on a smooth surface has only been reported quantitatively in the series of articles by Weiss et al. stated above that are based on experiments in one test facility. Furthermore, their experimental results are not fully consistent with the DNS results of Wu et al. (2020). Thus, it remains possible that the low-frequency unsteadiness observed experimentally may be caused by some sort of artefact from their configuration or from the test facility. Motivated by these doubts, we address the low-frequency behavior of a different type of pressure-induced TSB in the present study. Here, a two-dimensional diffuser induces an APG that leads to separation of the turbulent boundary layer. The reattachment process is not enforced by an FPG but is mainly governed by the orientation of the separating streamline with regard to the test surface. For this setup, low-frequency dynamics were revealed recently through a dynamical analysis of the wall shear-stress signature on the centre line (Weiss et al.,

2022). After addressing further aspects of this motion in the present setup, particular emphasis is put on accompanying spanwise low-frequency effects.

2. Methods

The experiments were conducted in a closed-loop, low-speed wind tunnel at a mean inflow velocity in the nozzle outlet plane $U_\infty = 20\,\text{m/s}$ ($Re_\theta \approx 5200$). The ceiling of the closed test section at $y = 400\,\text{mm}$ consisted of a flat plate while optical access was enabled through acrylic glass side walls at centre line distances of $\Delta z = \pm 300\,\text{mm}$. An APG was introduced by means of a linear widening of the test section at a diffuser angle of $\alpha = 20°$ as displayed in Figure 1 (upper left).
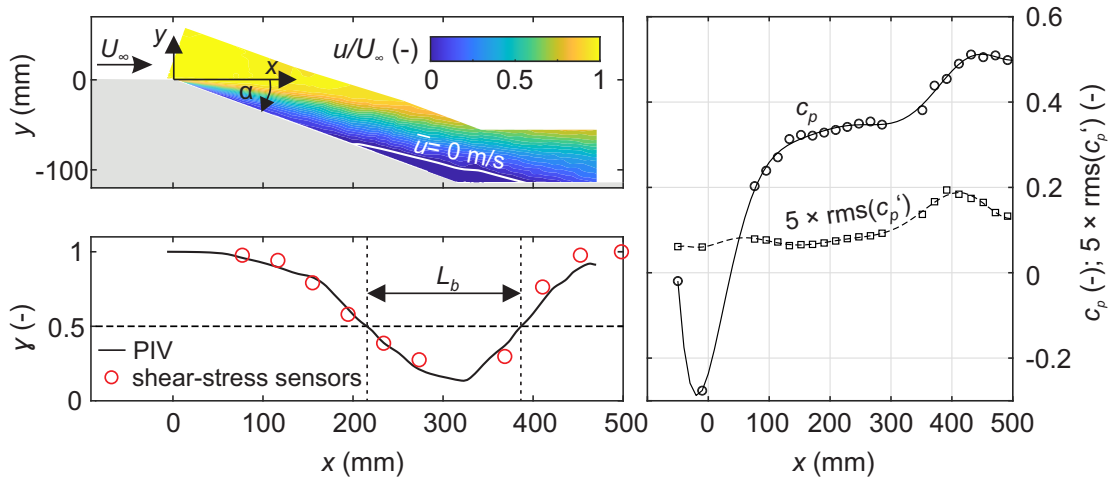

Figure 1. One-sided diffuser test section; mean streamwise velocity (upper left), forward-flow fraction along diffuser centre line (lower left), mean and fluctuating pressure distributions (right).

At the diffuser entrance, a smooth transition between horizontal inflow plate and diffuser ramp was designed to avoid geometry-induced flow separation. Here, the flow accelerates and a drop in static pressure is observed around $x \approx 0\,\text{mm}$ (right in Figure 1). Further downstream ($x \approx 0, \ldots, 150\,\text{mm}$), a strong APG develops before the pressure coefficient stagnates, indicating the presence of separated flow which is indeed confirmed by PIV measurements shown in the upper left. At $x \approx 400\,\text{mm}$, the separated shear layer reattaches, yielding a local maximum in pressure fluctuations. More detailed information regarding the near-wall flow direction is provided by considering the sign both of the near-wall velocity component u throughout the diffuser symmetry plane and the wall shear-stress at 10 sensor locations (bottom left of Figure 1). This allows to compute local forward-flow fractions γ that represent the relative amount of time where the flow is directed in positive x direction. Hence, values in the range $\gamma = 0, \ldots, 1$ can be measured with the boundaries indicating reverse-flow and forward-directed flow at all times, respectively. A fraction of $\gamma \approx 1$ is observed at the first sensor location, confirming that the flow only separates further downstream due to the presence of the APG. The region spanned by the TSB may be defined by values of $\gamma \leq 0.5$ that is enclosed by the locations of transitory detachment and reattachment (Simpson, 1989). In the current setup, a mean streamwise TSB dimension of $L_\text{b} \approx 0.18\,\text{m}$ is found.

Several experimental methods were applied during the course of this study. First, unsteady wall pressure measurements were performed at selected locations along the diffuser centre line using piezo-resistive pressure transducers with a range of up to $p \approx 6.9\,\text{kPa}$ and a sensitivity of $S \approx 25\,\text{mV/kPa}$. The cut-off frequency was approximately $f_{\text{c}} \approx 1.5\,\text{kHz}$, a strong anti-aliasing filter was used and a relatively long acquisition duration of $t_{\text{s}} = 180\,\text{s}$ was chosen to capture potential low-frequency fluctuations.

Furthermore, time-resolved PIV was performed to provide a data base to assess longitudinal velocity fluctuations by means of Spectral Proper Orthogonal Decomposition (SPOD) as explained in the next section. The two-component velocity field in the symmetry plane was measured with an acquisition rate of $f_{\text{s}} = 100\,\text{Hz}$ as two cameras with overlapping fields of view were used to cover the flow region in the range $x = 0, \ldots, 450\,\text{mm}$ with a spatial resolution of $\Delta x = \Delta y \approx 2.5\,\text{mm}$. In a second PIV arrangement, three-component velocity fields were measured in cross-sections at $x = (0, 72, 183, 326)\,\text{mm}$ in the $z > 0\,\text{mm}$ half-plane to reveal potential spanwise phenomena. Here, snapshots with a spatial resolution of $\Delta z = 1.8\,\text{mm}, \ \Delta y = 1.3\,\text{mm}$ were recorded for a duration of $t_{\text{s}} = 360\,\text{s}$ at a sample rate of $f_{\text{s}} = 6\,\text{Hz}$.

Simultaneous to stereoscopic PIV measurements, the wall shear-stress was measured on the diffuser centre line at $x \approx 195\,\text{mm}$, i.e. close to the location of transitory detachment. This enabled an assignment of individual PIV snapshots to the instantaneous velocity field in the symmetry plane with more details provided in the next section. The employed wall shear-stress sensor relies on a thermo-electrical function principle that is explained in detail by Weiss and co-workers (Weiss, Schwaab, et al., 2017; Weiss, Jondeau, et al., 2017). In the current study, no calibration is applied since only the sign of the output voltage was required to compute short-time forward-flow fractions γ', following a procedure that is inspired by the averaging method suggested by Eaton & Johnston (1982).

3. Results

In this section, we will first characterise the low-frequency *breathing* motion observed in the current setup. Then, attention is turned to spanwise effects linked to this phenomenon.

3.1. Low-frequency dynamics in diffuser symmetry plane

Based on pressure measurements with a duration of $t_s = 180\,\text{s}$, pre-multiplied power spectral densities (PSDs) were computed using Welch's modified periodogram method. These are presented in Figure 2 for selected locations. Recall that the Strouhal number $St = fL_{\text{b}}/U_\infty$ is based on the mean TSB length $L_{\text{b}} = 0.18\,\text{m}$ and the reference velocity $U_\infty = 20\,\text{m/s}$.

No significant frequency content is apparent inside the considered frequency range at $x \approx -49\,\text{mm}$ where the incoming turbulent boundary layer is attached and corresponding frequencies presum-
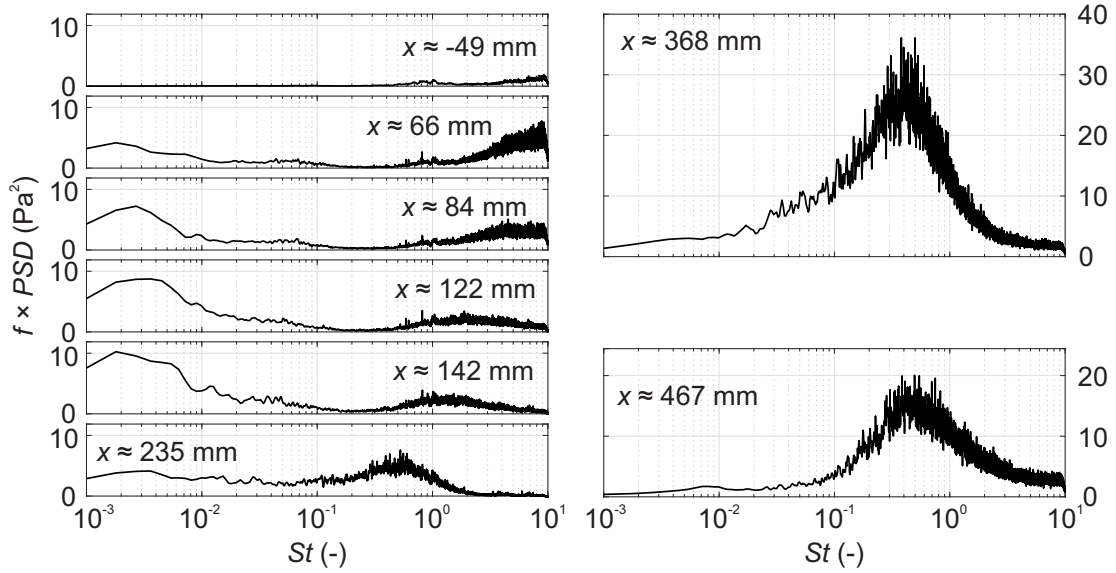
Figure 2. Pre-multiplied wall pressure spectra along the diffuser centre line.

ably exceed the bandwidth of the present setup. At $x \approx 66\,\text{mm}$, i.e. in the region of maximum APG, high-frequency fluctuations ($St > 1$) can be observed, which are linked to small-scale motion inside the turbulent boundary layer that is attached most of the time at this location. There is also a clear low-frequency hump at Strouhal numbers of $St < 0.01$, which becomes even more apparent slightly further downstream at $x \approx (84, 122, 142)\,\text{mm}$. In addition, the small-scale motion is associated with decreasing frequencies in streamwise direction as the boundary layer grows in thickness before separating from the wall. Downstream of the mean detachment location, at $x \approx 235\,\text{mm}$, the low-frequency hump is less distinct and medium-frequency fluctuations around $St \approx 0.5$ occur. These reflect the growth and merging of vortex structures inside the separated shear layer. Eventually, these vortex structures impinge on the wall ($x \approx 368\,\text{mm}$), and their footprint is clearly apparent in the medium-frequency regime at $St \approx 0.4$, equalling the value reported by Mohammed-Taifour & Weiss (2016). Further downstream ($x \approx 467\,\text{mm}$), the shedding frequency of vortex structures is still noticeable, albeit at a decreased amplitude.

Based on the pressure fluctuations presented above, we conclude that the TSB addressed in the present article exhibits similar characteristics as the one investigated by Weiss et al. (2015) despite considerable differences in the experimental setup. Specifically, we also measured low-frequency $\mathcal{O}(St) = 0.01$ pressure fluctuations inside the region of the largest APG. In order to relate these pressure fluctuations to a potential low-frequency motion of the flow field, we will now apply Spectral Proper Orthogonal Decomposition (SPOD) to fluctuations of the streamwise velocity component in the symmetry plane. Initially introduced by Lumley (1970), this method has gained some prominence recently thanks to the clarifications of Towne et al. (2018). As opposed to the 'classical' and 'snapshot' implementations of POD that may be considered space-only analyses, the space-time SPOD yields modes that oscillate at single frequencies and thus, lends itself to the dynamical analysis of the flow under consideration. Indeed, SPOD was recently applied with great success to the time-resolved wall shear-stress signature of the TSB in the present setup (Weiss et al., 2022).

In the current study, SPOD modes are computed using blocks of $N_f = 512$ snapshots that were recorded at an acquisition rate of $f_s = 100\,\text{Hz}$. The eigenvalue spectrum is shown as a function of the Strouhal number in the left of Figure 3. Note that the eigenvalues have been normalised by the total turbulent kinetic energy across all frequencies.
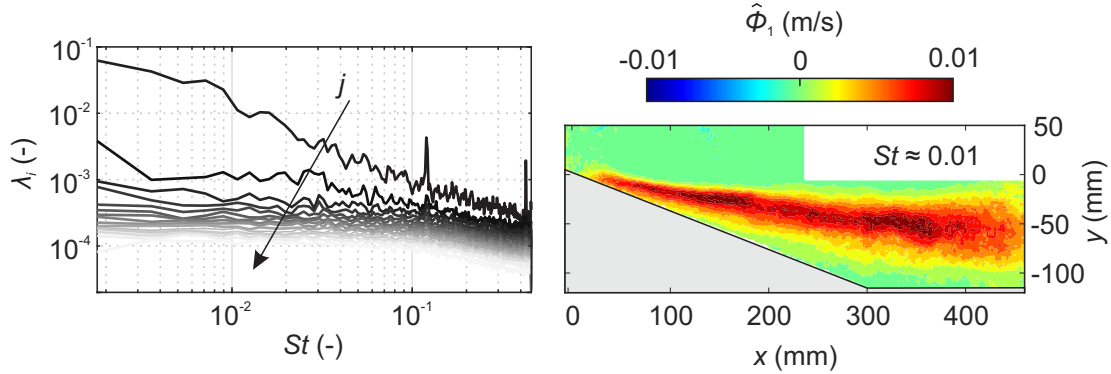

Figure 3. Normalized SPOD eigenvalue spectrum (left) and first SPOD mode at $St \approx 0.01$ (right).

Considering the low-frequency regime ($St < 0.1$), a distinct low-rank behavior can be noted as the leading mode captures significantly larger fractions of the total energy than the second mode. At $St = 0.01$, for instance, the most energetic mode ($j = 1$) contains approximately 70% of the total energy pertaining to this frequency. It is important to note that SPOD modes associated with a specific eigenvalue rank j do not necessarily capture the same dynamical events at different frequencies. However, in the present scenario, similar real parts of the velocity fluctuation field are observed inside the frequency range stated above. Interestingly, the representative example shown in the right of Figure 3 is reminiscent to the space-only POD mode presented by Mohammed-Taifour & Weiss (2016) for their TSB setup and is also found for the first space-only POD mode in the present work (not shown here).

To illustrate the physical meaning of this mode, we will now present a low-order model (LOM) that is based on the leading modes in the frequency range $St \approx 0.005, \ldots, 0.017$ ($f \approx 0.5, \ldots, 3\,\text{Hz}$). For this, the Fourier-transformed snapshot matrix required to compute the SPOD is first reconstructed with the leading modes only. This provides an LOM in Fourier space. Then, the Fourier coefficients at each spatial position in the PIV field of view are transformed into time signals via the inverse FFT, though only those components within the frequency range of interest ($f = 0.5, \ldots, 3\,\text{Hz}$) are considered while all other coefficients are set to zero. This way, only the first SPOD mode at each frequency within the selected range is used to build the LOM. To extract meaningful snapshots of this reconstructed series, we calculate an integral forward-flow fraction Γ taking into account all velocity vectors for each timestep of reconstructed velocity fields. Hence, a large value of Γ is assumed to indicate a contracted TSB, and a large Γ is used to identify timesteps where the TSB is expanded. We select the extrema of the forward-flow time series in Figure 11 (left), which roughly correspond to $t = 0.3\,\text{s}$ and $t = 1.75\,\text{s}$, and extract the snapshots of pertaining to these timesteps. The extreme representations of the flow topology are shown in Figure 11 (right).

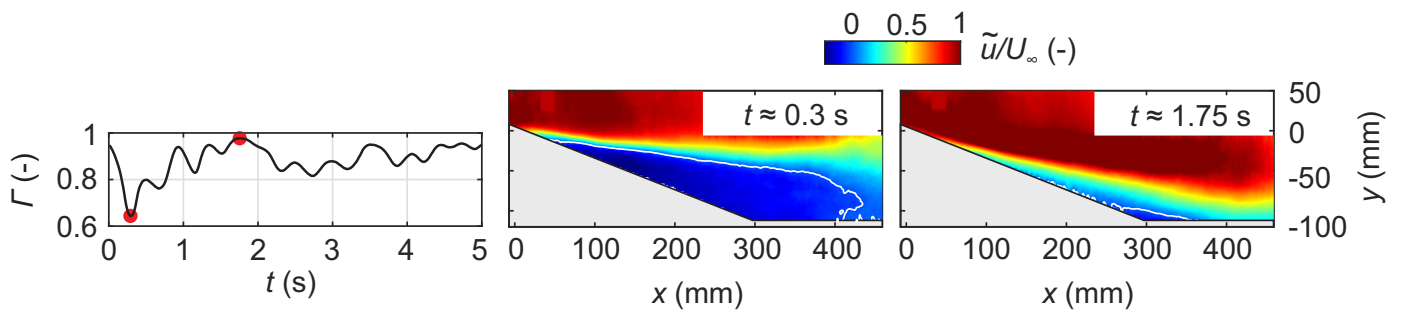**Figure 4.** Extreme representations of first POD mode in diffuser symmetry plane; for small integral forward-flow fraction Γ (left) for large Γ (right).

It is interesting to note that the forward-flow time series indicates the formation of a large TSB ($t < 0.5\,\mathrm{s}$) as an exceptional event whereas for the remainder of the time, a fluctuation of Γ around a mean value of approximately $\overline{\Gamma} = 0.9$ is apparent.

3.2. Low-frequency dynamics in cross-sections

Now, we will address spanwise flow effects and attempt to relate them to the low-frequency dynamics presented above. The mean streamwise velocity component $\bar{u}$ in four cross-sections is shown in Figure 5.
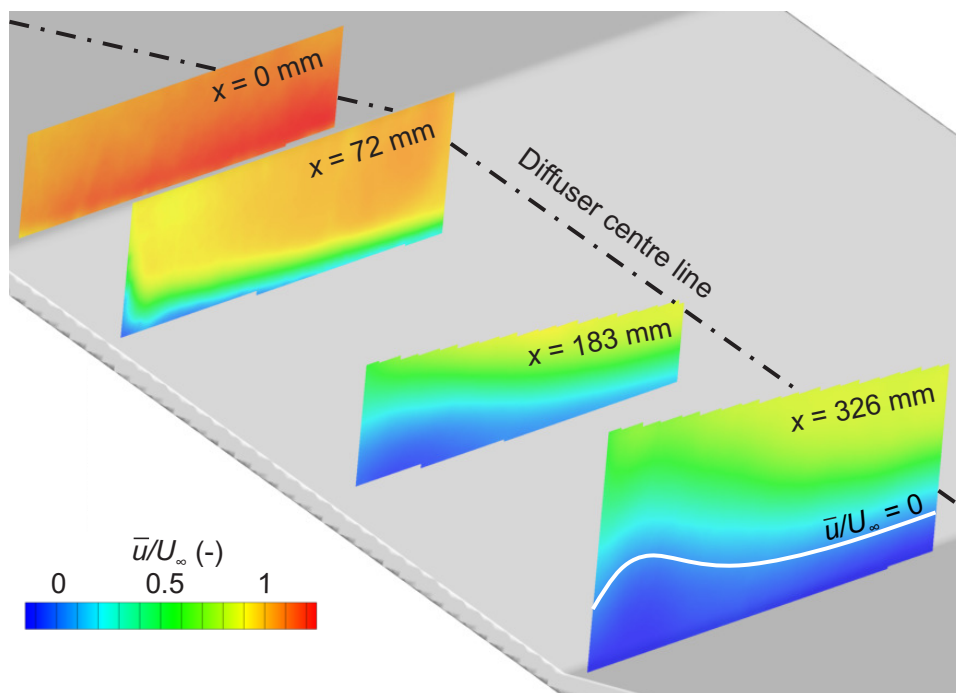

Figure 5. Mean streamwise velocity distributions in four cross-sections along the diffuser.

Consistent with the pressure drop displayed in Figure 1, a velocity larger than U_∞ is observed at $x = 0\,\mathrm{mm}$ near the symmetry plane while the velocity decreases with greater centre line distance. Due to the APG, a thicker boundary layer is observed in the second cross-section ($x = 72\,\mathrm{mm}$).

Again, the velocity contour is not homogeneous in spanwise direction as a stronger velocity deficit can be noted near the side wall. The same is true at $x = 183\,\text{mm}$ where a region with $\bar{u} \to 0\,\text{m/s}$ of large vertical extent is found near the side wall. At the diffuser foot ($x = 326\,\text{mm}$), the mean streamwise velocity close to the wall is negative throughout the cross-section, again with a velocity deficit that is more distinct near the side wall.

Since the modal decomposition was proven to capture the low-frequency dynamics in the symmetry plane, we will now apply space-only POD to streamwise velocity fluctuations in the cross-sections located at $x = (183, 326)\,\text{mm}$, i.e. near the mean separation line and inside the TSB, respectively. Recall that the acquisition frequency was only $f_\text{s} = 6\,\text{Hz}$ for these measurements, preventing a spectral analysis that was presented for the symmetry plane above. The most dominant spatial modes for both cross-sections are shown in Figure 6.
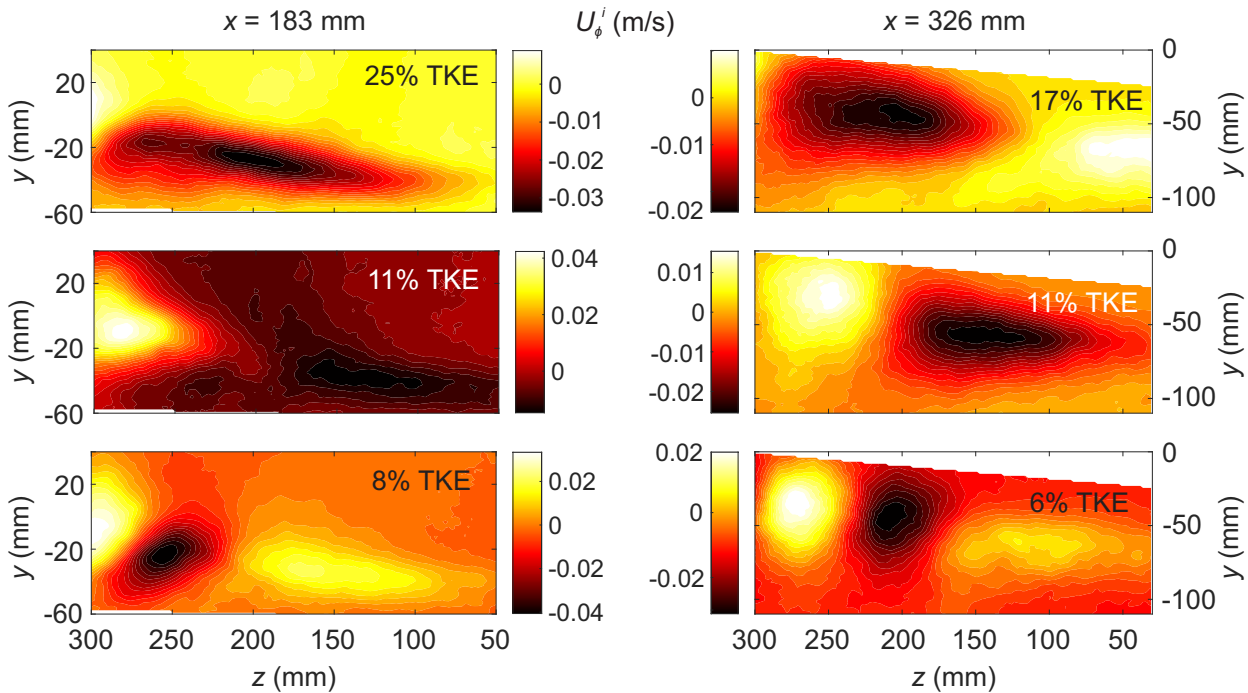

Figure 6. First three spatial POD modes in cross-section located at $x = 183\,\text{mm}$ (left column) and $x = 326\,\text{mm}$ (right column).

At $x = 183\,\text{mm}$, 25% of the turbulent kinetic energy is represented by a first mode that appears to be consistent with the most dominant mode in the symmetry plane (Figure 3). Here, velocity fluctuations are rendered by a large-scale region that is aligned with the boundary layer as it grows away from the wall towards the side wall at $z = 300\,\text{mm}$. The second and third mode contain anti-correlated regions of velocity fluctuations alternating in spanwise direction at different wavelengths, which can also be observed in the spatial modes at $x = 326\,\text{mm}$ (right column). It is important to note that these regions are associated with modal velocities of opposite sign. Hence, according to the first mode at $x = 326\,\text{mm}$ for instance, a reduced instantaneous velocity near the side wall ($z > 150\,\text{mm}$) is accompanied by a velocity increase near the symmetry plane, and vice versa. The implications of these anti-correlated fluctuations will be revisited later on in this paper.

To estimate whether the POD modes presented above are physically relevant (and not merely a result of enforced statistical optimality), we will assess the extremum states of the TSB provided by two different approaches. First, cross-section velocity fields at $x = (183, 326)\,\text{mm}$ will be considered only for temporal coefficients of the first POD modes a_1 that are 20% within the respective minimum and maximum. In practice, we define threshold values $a_{1,\text{low}}$ and $a_{1,\text{high}}$ and compute ensemble-averaged velocity fields based on instantaneous distributions where a_1 is smaller/larger than these values. It is important to note that this method does not allow conclusions regarding the frequency associated with fluctuations captured by the first POD mode, nor is it relatable to flow events on the symmetry plane that has been considered to assess TSB low-frequency dynamics in previous studies. Therefore, we will pursue a second method of snapshot selection that is based on the information of a wall shear-stress sensor located on the centre line near the mean separation point. We will briefly provide some further details on this approach before comparing the velocity fields obtained through both methods.

An exemplary time signal of the wall shear-stress sensor at $x = 195\,\text{mm}$ is shown in the left diagram of Figure 7.
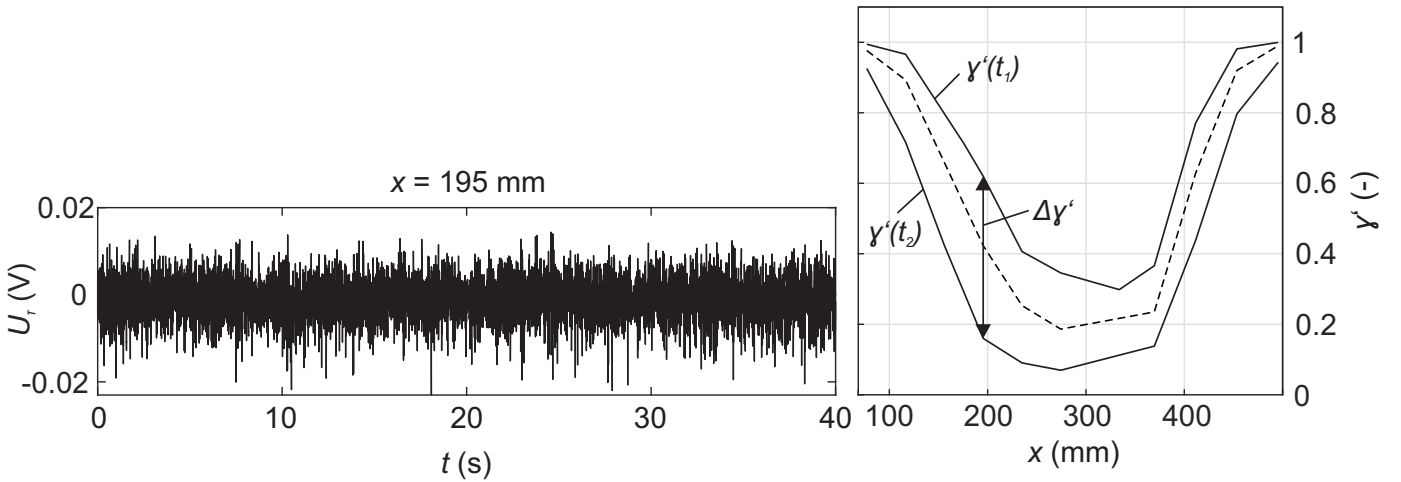

Figure 7. Exemplary output voltage signal of wall shear-stress sensor located at $x = 195\,\text{mm}$ (left) and selected short-time forward-flow fraction distributions γ' throughout the diffuser (right).

Note that a positive voltage is induced by wall shear-stress directed in the main flow direction while negative output voltage can be attributed to reverse-flow. As a means of low-pass filtering, we compute short-time forward-flow fractions γ' based on signal segments of $\Delta t = 0.5\,\text{s}$ (2500 samples). This duration was chosen because it approximately corresponds to the low-frequency hump associated with the *breathing* phenomenon determined through pressure measurements and SPOD in the previous section. The diagram in the right of Figure 6 contains distributions of short-time forward-flow fractions for time instances t_1 and t_2 where γ' reaches its maximum/minimum at $x = 195\,\text{mm}$ along with the mean distribution (dashed line). The sensor location at $x = 195\,\text{mm}$ features the largest range in γ' due to the proximity to the mean separation line. It is also worth mentioning that the short-time forward-flow fractions are correlated throughout the centre line due to the global character of the low-frequency TSB dynamics. As a result, one wall shear-stress

sensor (at $x = 195\,\mathrm{mm}$) is sufficient to make conclusions regarding the streamwise TSB extent.

To identify cross-section velocity fields related to extremum TSB states based on this wall shear-stress sensor, let us first consider the histogram of γ' shown in Figure 8 (left).
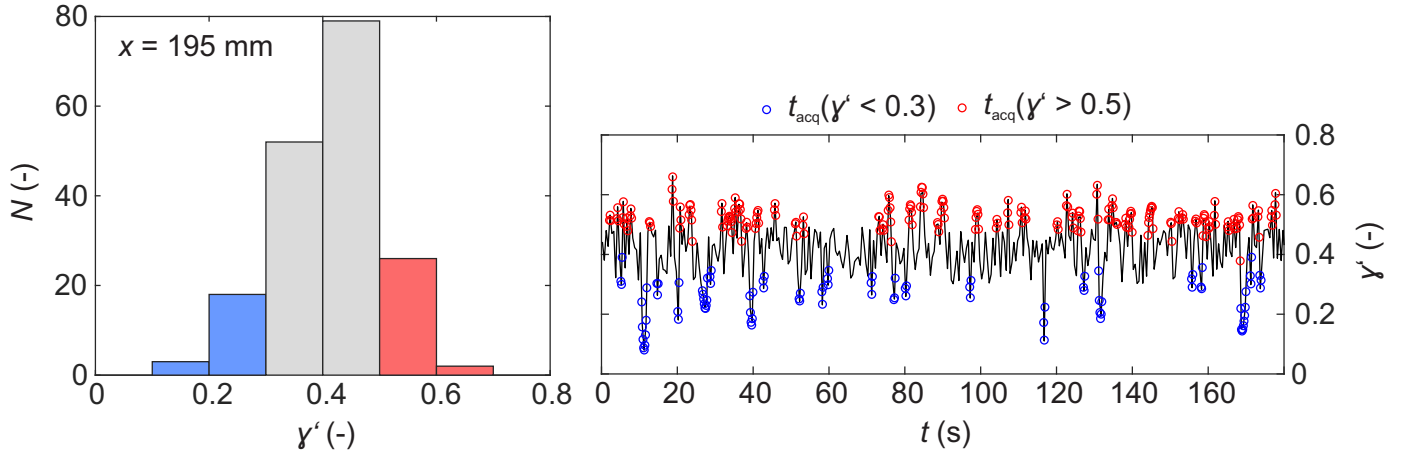

Figure 8. Histogram for sensor located at $x = 195\,\mathrm{mm}$ (right) and exemplary time signal of short-time forward-flow fraction and PIV snapshot acquisition times for $\gamma' > 0.5$ (red circles) and $\gamma' < 0.3$ (blue circles).

A distribution around a mean value of $\gamma' \approx 0.4$ can be noted. Extremum forward-flow fractions are now arbitrarily defined as $\gamma' < 0.3$ and $\gamma' > 0.5$, and PIV snapshots are picked from the associated time intervals. This is illustrated in the right of Figure 8 where snapshot acquisition times t_{acq} for small/large γ' are marked by blue/red circles.
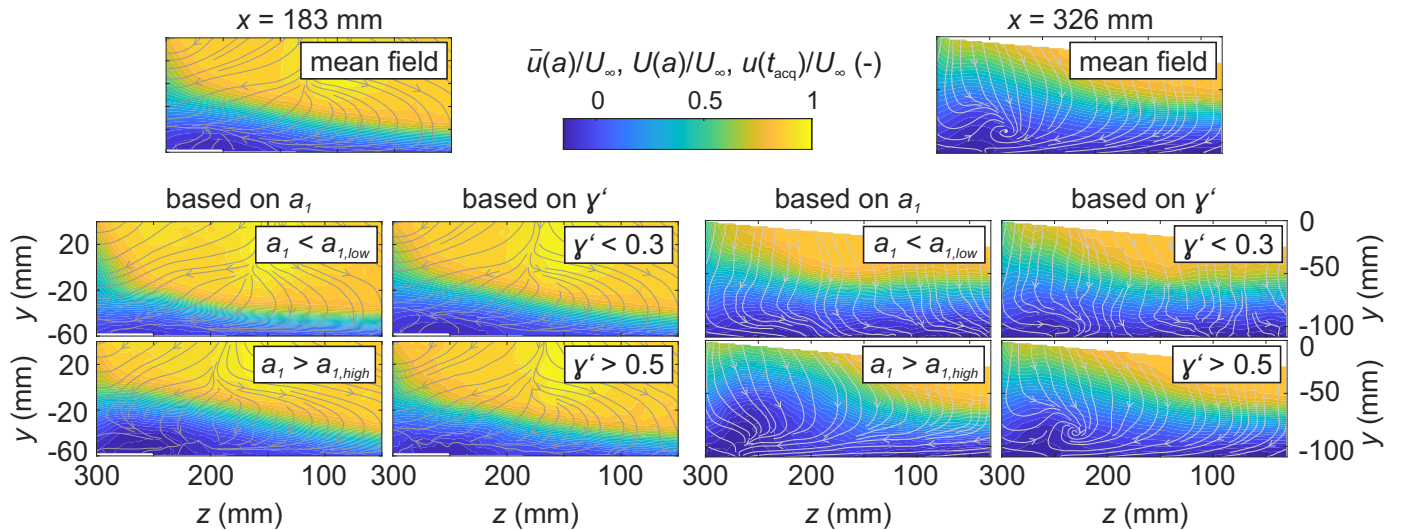

Figure 9. Mean streamwise velocity and in-plane streamlines inside cross-sections located at $x = 183\,\mathrm{mm}$ (left) and $x = 326\,\mathrm{mm}$ (right); mean velocity fields in the top row; bottom rows: snapshot selection either based on value of first POD temporal coefficient a_1 or short-time forward-flow fraction γ'.

Following the method introduced above, ensemble-averaged velocity fields are computed for time instances $t_{\mathrm{acq}}(\gamma' < 0.3)$ and $t_{\mathrm{acq}}(\gamma' > 0.5)$, respectively. Along with the POD-based snapshot selection where instantaneous velocity fields are considered at acquisition times $t_{\mathrm{acq}}(a_1 > a_{1,\mathrm{high}})$ or

$t_{acq}(a_1 < a_{1,\text{low}})$, these velocity fields are shown in Figure 9. Note that the mean velocity fields, taking into account all 2160 snapshots, are shown in the top row for reference.

As for the location near the mean separation line ($x = 183\,\text{mm}$), a stronger velocity deficit in the near-wall region is at hand for $a_1 > a_{1,\text{high}}$ compared to the case of small POD coefficients (first column). For the γ'-based snapshot selection, there appears to be no significant difference between the cases of $\gamma' < 0.3$ and $\gamma' > 0.5$ although a slight effect will be presented in due course. In the case of the cross-section at $x = 326\,\text{mm}$, a distinct effect can be noted: both for small a_1 and small γ', the velocity deficit near the side wall that is also present in the mean field is diminished to some extent. At the same time, the near-wall outward-directed velocity component (in z direction) is suppressed, if not reversed. For large a_1 and γ', on the other hand, the velocity field is similar to the mean field inasmuch as the velocity deficit grows with increasing distance to the symmetry plane and a longitudinal vortex structure is found with its core at $z \approx 250\,\text{mm}$. It is also interesting to note that the averaged velocity fields based on POD and wall shear-stress measurements are very similar. This suggests that the temporal coefficient for the first POD mode a_1 and the short-time forward-flow fraction γ' must be correlated, which is confirmed in Figure 10 where both quantities are plotted in normalised form for an exemplary time segment.
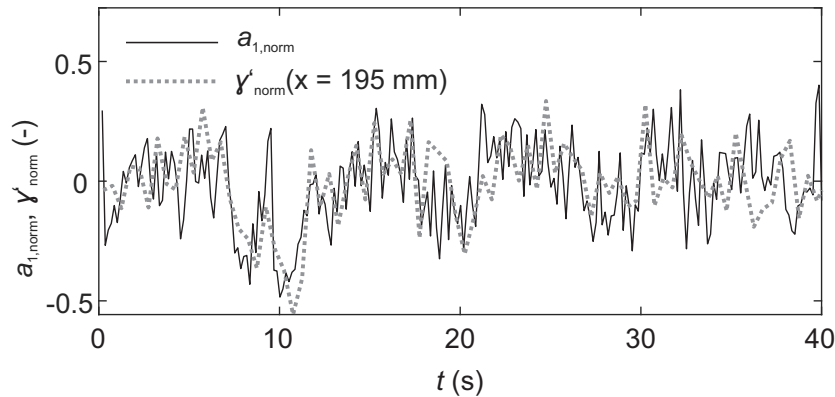

Figure 10. Time signals of normalised short-time forward flow fraction and temporal coefficient of first POD mode.

There is a linear correlation between the two signals, which is reflected in correlation coefficients of $R \approx 0.4$ for the cross-section at $x = 183\,\text{mm}$ and $R \approx 0.5$ at $x = 326\,\text{mm}$. As a consequence, the probability of reverse-flow in the symmetry plane is reduced for large a_1 because then, γ' also tends to assume large values. Revisiting the first POD mode at $x = 326\,\text{mm}$ (Figure 6), a large/positive temporal coefficient indeed results in transient increases of the velocity near the symmetry plane. At the same time, the velocity near the side wall is reduced, which will now be addressed in more detail based on velocity profiles extracted from the velocity fields shown in Figure 9. For each streamwise location $x = (183, 326)\,\text{mm}$, profiles representative of the flow near the symmetry plane ($z = 50\,\text{mm}$) and near the side wall ($z = 250\,\text{mm}$) are displayed.

Note that the mean velocity profiles, averaged over all snapshots, are highlighted by dashed lines. Interestingly, the mean profiles are almost identical to those obtained for $\gamma' > 0.5$ (red lines). In other words, there is no marked difference between the mean flow field and time instances of
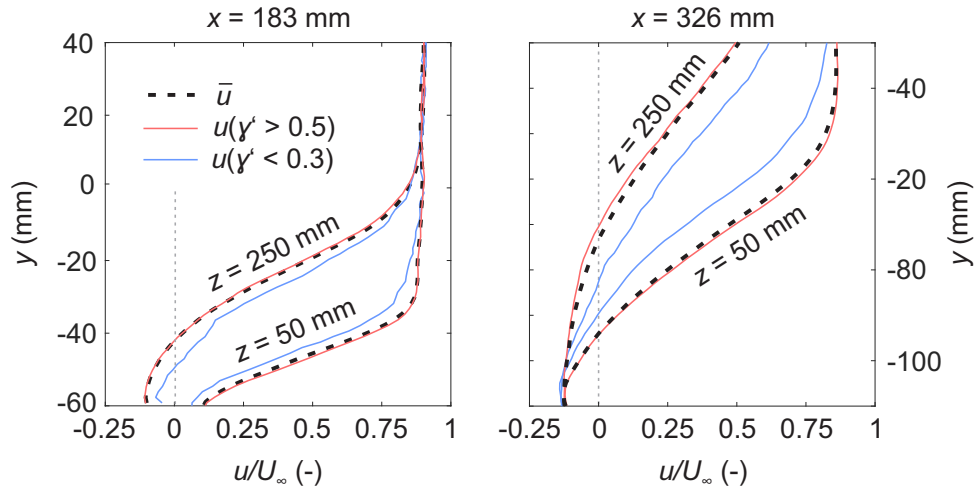
Figure 11. Mean streamwise velocity profiles at $z = (50, 250)\,\mathrm{mm}$ in cross-sections located at $x = 183\,\mathrm{mm}$ (left) and $x = 326\,\mathrm{mm}$ (right).

large short-time forward flow fractions, which is consistent with the skewed distribution shown in Figure 8. For $\gamma' < 0.3$, however, a different picture is revealed (blue lines). While the streamwise velocity near the side wall is increased, a drop in velocity can be noted near the symmetry plane, which is particularly noticeable inside the TSB ($x = 326\,\mathrm{mm}$). This effect is fully consistent with the first POD mode (Figure 6) containing two large-scale regions of anti-correlated velocity fluctuations near the symmetry plane and near the side wall, respectively.

Based on the results presented above, we conclude that the probability of reverse-flow is increased during relatively rare time intervals that occur non-periodically (Figure 8). Here, the outward-directed velocity component is suppressed and the streamwise vortex that is also present in the mean velocity field is absent. To gain a better understanding of these flow structures, an oil-film visualisation of the diffuser surface is presented in Figure 12. Note that the locations of measurement planes evaluated above are highlighted by green lines while the locations of transitory detachment x_s and reattachment x_r in the symmetry plane highlighted by dashed lines.

The oil-film pattern clearly reveals the footprints of two symmetric side wall vortices that are associated with inward-directed velocity on the top part of the diffuser ramp before the sign of the mean spanwise velocity component appears to change, which is confirmed by PIV measurements where $\bar{w} \approx 0.1 U_\infty$ is determined in the near-wall region at $x = 326\,\mathrm{mm}$. Since this velocity component is suppressed during time intervals where $\gamma' < 0.3$, we hypothesise that the entire side wall vortex may be diminished, which is associated with the temporary presence of a TSB of increased dimensions.

4. Conclusions

The objective of this study was to identify and characterise low-frequency dynamics pertaining to a pressure-induced TSB with particular emphasis on potential three-dimensional flow effects.
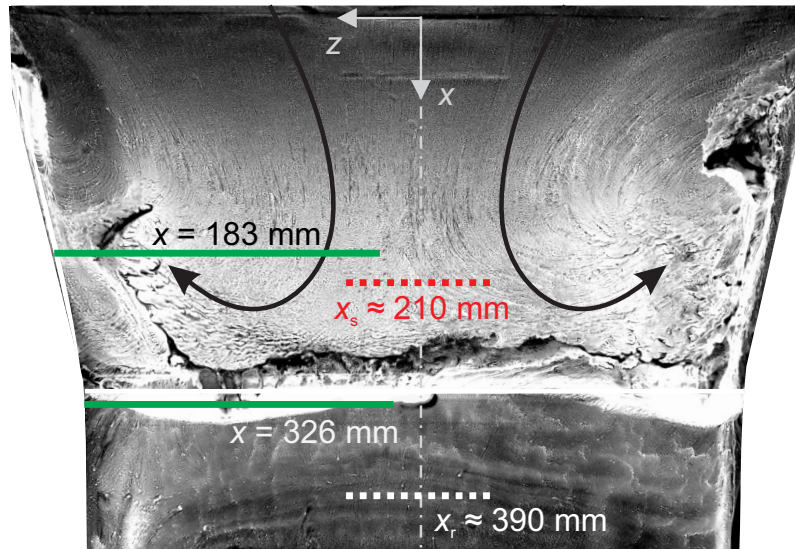
Figure 12. Oil film visualisation on diffuser surface; locations of two PIV measurement planes highlighted by green lines, locations of transitory detachment x_s and reattachment x_r in the symmetry plane highlighted by red/white dashed lines.

To this end, experiments were conducted in a low-speed wind tunnel and various aspects of the flow were assessed, including the time-resolved wall pressure signature in the centre line, the time-resolved velocity field in the symmetry plane as well as (non-time-resolved) velocity fields in several cross-sections inside one half-plane of the diffuser.

A low-frequency motion, similiar to the one reported by Mohammed-Taifour & Weiss (2016) in a different experimental setup, was also observed in the present work. As was the case in the study mentioned above, this phenomenon is manifested in pressure fluctuations at $\mathcal{O}(St) = 0.01$ in the region of the largest APG. Frequency content on the same order of magnitude is also revealed by means of SPOD (Towne et al., 2018). This method has recently been shown to be suited to investigate TSB low-frequency dynamics when applied to the wall shear-stress signature on the centre line by Weiss et al. (2022). In the present article, the statistical base is provided in the form of fluctuations of the streamwise velocity component in the symmetry plane, and very dominant modes are found in the low-frequency regime with a structure that is reminiscent of the first spatial space-only POD mode presented by Mohammed-Taifour & Weiss (2016), capturing a large-scale longitudinal contraction/expansion of the TSB. Space-only POD was then applied to the velocity fields measured in cross-sections located near the mean separation line and inside the TSB, respectively. Here, the acquisition frequency was not sufficient to conduct a dynamical analysis directly. However, it was shown that the temporal coefficients associated with the most dominant mode are correlated with the low-frequency wall shear-stress information on the centre line. Thus, flow states observed in cross-section velocity fields could be related to the *breathing* motion unfolding in the symmetry plane by means of ensemble-averaging. As the major finding of this article, we noted that mean cross-section velocity fields in the TSB are characterized by a strong outward-directed velocity component as well as a longitudinal vortex structure near the diffuser side wall.

These characteristics are also at hand for the TSB in its contracted state. During the expanded state, however, both the side wall vortex and the outward-directed velocity component are suppressed. At the same time, the velocity deficit near the side wall is reduced while the streamwise velocity near the symmetry plane drops below the value found for the mean flow field.

Based on the inspection of the wall shear-stress signal, the suppression of the side wall vortex can be referred to as a non-periodic and relatively rare event, hence falling into the low-frequency regime. The results presented in this article suggest that the *breathing* motion of the TSB is associated with these events and may therefore be considered a fully three-dimensional phenomenon. It remains unclear, however, if the origin of this motion is linked to the presence of the sidewalls or not.

Acknowledgements

Nomenclature

a_j	j^{th} modal expansion coefficient (-)
$a_{1,\text{low}}$, $a_{1,\text{high}}$	Threshold values of first modal expansion coefficient (-)
$a_{1,\text{norm}}$	Normalized first modal expansion coefficient (-)
f	Frequency (s^{-1})
f_c	Cut-off frequency (s^{-1})
f_s	Sample rate (s^{-1})
j	Mode number (-)
L_b	Length of turbulent separation bubble (m)
N	Number of snapshots (-)
p	Pressure (Pa)
R	Normalized correlation coefficient (-)
Re_θ	Reynolds number based on momentum thickness (-)
S	Sensitivity of pressure transducer (V/Pa)
St	Strouhal number (-)
t	Time (s)
t_acq	Acquisition time instant (s)
t_s	Measurement duration (s)
U_τ	Sensor output voltage (V)
U_∞	Free stream velocity (m/s)
u, v, w	Velocitiy components in Cartesian coordinates (m/s)
$\tilde{u}$	Streamwise velocity of low-order model (m/s)

x, y, z	Cartesian coordinates (m)
$x_\mathrm{s}, x_\mathrm{r}$	Locations of transitory detachment and reattachment (m)
α	Diffuser opening angle (deg)
Γ	Integral forward-flow fraction (deg)
γ	Forward-flow fraction (deg)
γ'	Short-time forward-flow fraction (-)
γ'_norm	Normalized short-time forward-flow fraction (-)
Δt	Time interval (s)
$\Delta x, \Delta y, \Delta z$	Distances in Cartesian coordinates (m)
$\Delta \gamma'$	Range of short-time forward-flow fractions (-)
λ_j	j^th eigenvalue ($\mathrm{m^2/s^2}$)
$\hat{\Phi}_j$	j^th SPOD mode (m/s)

References

Camussi, R., Felli, M., Pereira, F., Aloisio, G., & Marco, A. D. (2008). Statistical properties of wall pressure fluctuations over a forward-facing step. *Phys. Fluids*, *20*(7).

Cherry, N. J., Hillier, R., & Latour, M. E. M. P. (1984). Unsteady measurements in a separated reattaching flow. *J. Fluid Mech.*, *144*, 13–46.

Clemens, N. T., & Narayanaswamy, V. (2014). Low-frequency unsteadiness of shock wave/turbulent boundary layer interactions. *Annu. Rev. Fluid Mech.*, *46*, 469–492.

Dianat, M., & Castro, I. P. (1991). Turbulence in a separated boundary layer. *J. Fluid Mech.*, *226*, 91–123.

Driver, D. M., Lee Seegmiller, H., & Marvin, J. G. (1987). Time-dependent behavior of a reattaching shear layer. *AIAA J.*, *25*(7), 914–919.

Dussauge, J.-P., Dupont, P., & J.-F.Debiève. (2006). Unsteadiness in shock wave boundary layer interactions with separation. *Aerosp. Sci. Tech.*, *10*(2), 85–91.

Eaton, J. K., & Johnston, J. P. (1982). Low frequency unsteadiness of a reattaching turbulent shear layer. In *Turbulent shear flows 3* (Vol. 2, p. 162-170). Davis, CA, United States.

Fang, X., & Tachie, M. F. (2020). Spatio-temporal dynamics of flow separation induced by a forward-facing step submerged in a thick turbulent boundary layer. *J. Fluid Mech.*, *892*.

Hain, R., Kähler, C. J., & Radespiel, R. (2009). Dynamics of laminar separation bubbles at low-reynolds-number aerofoils. *J. Fluid Mech.*, *630*, 129–153.

Hudy, L. M., Naguib, A. M., & W. M. Humphreys, J. (2003). Wall-pressure-array measurements beneath a separating/reattaching flow region. *Phys. Fluids*, *15*(3), 706–717.

Kiya, M., & Sasaki, K. (1983). Structure of a turbulent separation bubble. *J. Fluid Mech.*, *137*, 83–113.

LeFloc'h, A., Weiss, J., Mohammed-Taifour, A., & Dufresne, L. (2020). Measurements of pressure and velocity fluctuations in a family of turbulent separation bubbles. *J. Fluid Mech.*, *902*, A13.

Lumley, J. L. (1970). *Stochastic tools in turbulence*. New York: Academic Press.

Marxen, O., & Henningson, D. S. (2011). The effect of small-amplitude convective disturbances on the size and bursting of a laminar separation bubble. *J. Fluid Mech.*, *671*, 1–33.

Michelis, T., Yarusevych, S., & Kotsonis, M. (2017). Response of a laminar separation bubble to impulsive forcing. *J. Fluid Mech.*, *820*, 633–666.

Mohammed-Taifour, A., & Weiss, J. (2016). Unsteadiness in a large turbulent separation bubble. *J. Fluid Mech.*, *799*, 383–412.

Na, Y., & Moin, P. (1998). Direct numerical simulation of a separated turbulent boundary layer. *J. Fluid Mech.*, *374*, 379–405.

Simpson, R. L. (1989). Turbulent boundary-layer separation. *Annu. Rev. Fluid Mech.*, *21*, 205–232.

Towne, A., Schmidt, O. T., & Colonius, T. (2018). Spectral proper orthogonal decomposition and its relationship to dynamic mode decomposition and resolvent analysis. *J. Fluid Mech.*, *847*, 821–867.

Weiss, J., Jondeau, E., Giani, A., Charlot, B., & Combette, P. (2017). Static and dynamic calibration of a MEMS calorimetric shear-stress sensor. *Sensor Actuat. A: Phys.*, *265*, 211–216.

Weiss, J., Little, J., Threadgill, J., & Gross, A. (2021). *Low-frequency unsteadiness in pressure-induced separation bubbles (AIAA 2021-1324)*.

Weiss, J., Mohammed-Taifour, A., & Schwaab, Q. (2015). Unsteady behavior of a pressure-induced turbulent separation bubble. *AIAA J.*, *53*(9), 2634–2645.

Weiss, J., Schwaab, Q., Boucetta, Y., Giani, A., Guigue, C., Combette, P., & Charlot, B. (2017). Simulation and testing of a MEMS calorimetric shear-stress sensor. *Sensor Actuat. A: Phys.*, *253*, 210–217.

Weiss, J., Steinfurth, B., Chamard, L., Giani, A., & Combette, P. (2022). Spectral proper orthogonal decomposition of unsteady wall shear stress under a turbulent separation bubble. *AIAA Journal*, *60*(4).

Wu, W., Meneveau, C., & Mittal, R. (2020). Spatio-temporal dynamics of turbulent separation bubbles. *J. Fluid Mech.*, *883*(A45).